An Equivalent Skin-friction Coefficient for Parasite Drag Estimation and study of Its Influence on the Conceptual Design of Small Electric UAVs

Sidi Moulaye Sidi Moulay * and Mohamed Elamine Ait Ali

Université Mohammed V de Rabat, Ecole Mohammadia d'Ingénieurs, ERG2(ME), Rabat, Morocco
Email: sidnesidimoulaye@gmail.com (S.M.S.M); aitali@emi.ac.ma (M.E.A.A)
*Corresponding author

***Abstract*—The equivalent skin-friction method is widely used for parasite drag estimation during the conceptual design of small Unmanned Aerial Vehicles (UAVs). This study derives a new equivalent skin-friction coefficient for short-range electric mini UAVs using Computational Fluid Dynamics (CFD) simulations of nine representative UAV configurations. The derived coefficient is found to be significantly lower than values commonly adopted in the literature for UAV preliminary sizing. To evaluate its practical implications, the coefficient is incorporated into a conceptual sizing framework and applied to a representative design case. The results show that the use of conventional coefficients leads to systematic overestimation of parasite drag, affecting wing loading, power loading, and overall vehicle sizing. The proposed coefficient provides a more realistic basis for drag estimation and can improve the accuracy of conceptual design methods for electric mini UAVs.**

***Keywords*—parasite drag, equivalent skin friction, Unmanned Aerial Vehicles (UAVs), conceptual design, Computational Fluid Dynamics (CFD)**

I. Introduction

Electric Unmanned Aerial Vehicles (E-UAVs) represent one of the fastest-growing segments of the aerospace sector, with a reported Compound Annual Growth Rate (CAGR) of 16.6% between 2023 and 2028. This growth is driven primarily by the increasing demand for environmentally friendly aerial systems across multiple sectors [1]. Furthermore, advances in miniaturized avionics, electric propulsion, and battery technologies have enabled the development of small electric UAVs particularly suitable for a wide range of applications due to their compact size, low cost, and low acoustic and thermal signatures [2]. As the adoption of these platforms expands, the need for efficient sizing methodologies during the conceptual design phase becomes essential. Consequently, significant research efforts have been devoted to improve preliminary sizing approaches for small electric UAVs [3–5].

During the early stages of conceptual design, only limited information regarding the aircraft geometry and aerodynamic characteristics is available [6]. Consequently, simplified analytical and semi-empirical formulations are commonly employed to estimate key aerodynamic parameters such as lift and drag coefficients, based primarily on mission requirements and preliminary geometric assumptions. Among these parameters, parasite drag represents a particularly important aerodynamic quantity because it directly affects propulsion sizing, endurance, energy consumption, and overall UAV performance. One of the most widely used approaches for parasite drag estimation is the component drag build-up method [7–9], in which the total parasite drag is decomposed into contributions associated with the wing, fuselage, empennage, and other aircraft components. However, the analytical correlations employed in conventional component build-up methods were originally developed for manned aircraft and may not accurately represent the aerodynamic characteristics of small UAVs. Recent studies addressing the aerodynamics of small UAVs frequently rely on this method [10, 11]. Although these methods can provide reasonable drag predictions, they require detailed geometric information that is often unavailable during the early design stages. Moreover, a previous study [12] concluded that conventional component-based formulations are not always suitable for small-scale UAVs. Notably, Sahraoui *et al.* [13] developed an automated design and optimization framework for mini UAVs; however, their parasite drag estimation methodology relies on Gudmundsson's formulation [14], which represents a simplified component-based method that emphasizes wing relative to the remaining aircraft components.

An alternative approach is the Equivalent Skin Friction (ESF) method [15], which provides a practical

Manuscript received April 15, 2026; revised May 26, 2026; accepted August 5, 2026; published October 23, 2026.

compromise between simplicity and accuracy. Unlike component build-up methods, the ESF formulation estimates parasite drag using only two primary parameters: the aircraft wetted area and an equivalent skin-friction coefficient representative of a given aircraft category. This equivalent coefficient is an empirical parameter that represents the overall parasite drag, implicitly accounting for skin-friction, pressure (form), and interference drag contributions. Raymer [7] proposed representative ESF coefficients for several categories of conventional manned aircraft, while Götten *et al.* [16] later derived a dedicated coefficient for Short- and Medium-Range (SMR) fixed-wing UAVs. Their study involved a numerical aerodynamic analysis of ten UAV configurations considered representative of the SMR UAV class, which combines short-range and medium-range tactical UAV categories. The parasite drag of each configuration was evaluated and subsequently used to derive a dedicated equivalent skin-friction coefficient for this UAV class. Their parasite drag breakdown analysis indicated that approximately 27% of the total parasite drag originated from the landing gear system. However, small electric UAVs differ significantly from the tactical UAV configurations considered in Götten *et al.* [16]. Most small UAVs are hand-launched or catapult-launched and therefore do not incorporate landing gear systems. In addition, their lower cruise speeds correspond to substantially lower Reynolds numbers, leading to different boundary-layer characteristics and aerodynamic behavior. Consequently, the significant contribution of landing gear drag observed in Götten *et al.* [16] suggests that the derived SMR coefficient may not be appropriate for smaller, gearless UAV configurations. Furthermore, a review of the available literature indicates that no dedicated equivalent skin-friction coefficient has yet been derived specifically for small electric fixed-wing UAVs.

To address this gap, the present study derives a class-specific equivalent skin-friction coefficient for small electric fixed-wing UAVs through high-fidelity CFD simulations of nine representative UAV configurations. The considered UAV category consists of small electric fixed-wing UAVs falling within the mini-UAV class [17], generally characterized by a Maximum Take-Off Weight (MTOW) below 25 kg and an endurance of less than 2 h. Within this class, the UAVs considered in the present study are further characterized by the absence of landing gear, low cruise speeds, and short operational ranges typically below 20 km. Representative platforms such as the Biodrone and Azimut 2 [18] illustrate the general characteristics of this class. The numerical results reveal that the wing is the dominant contributor to parasite drag, unlike the trends reported for larger tactical UAVs. The derived ESF coefficient is significantly lower than the value proposed by Götten *et al.* [16] and differs from the coefficients commonly adopted for light manned aircraft. To evaluate the practical implications of these differences, the coefficient is incorporated into a conceptual design framework and applied to a representative sizing case study. The results demonstrate that the use of existing coefficients leads to a systematic overestimation of parasite drag and consequently affects wing and propulsion system sizing. The proposed coefficient therefore provides a more representative basis for parasite drag estimation and contributes to improving the accuracy of conceptual design methodologies for small electric UAVs.

II. Materials and Methods

A. Selection of Representative UAV Configurations

Despite the scarcity of publicly available detailed geometric data for small UAVs, from various reliable sources [19–21]. From this database, nine fixed-wing small electric UAVs were selected as representative configurations. The selection covers a broad range of configurations (see Fig. 1), including

- Tail designs: conventional tails, inverted V-tails, twin-booms, and V-tails;
- Wing types: straight wings, tapered wings, swept wings, dihedral wings;
- Wing positions: high-wing, low-wing, and mid-wing.

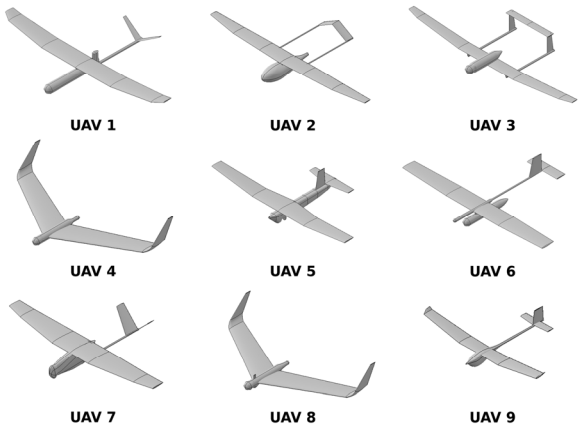

Fig. 1. Reconstructed OpenVSP models of the nine representative mini electric UAV configuration.

The UAV geometries were reconstructed in OpenVSP using dimensions obtained from manufacturers' technical specifications and published literature. When complete geometric information was unavailable, missing dimensions were estimated from available photographs and scaling relationships based on known dimensions. Table I summarizes the principal specifications of the selected UAVs.

Although the models do not precisely replicate the internal or structural details of the real aircraft, care was taken to preserve overall proportions and surface continuity. Minor angular distortions were corrected where possible. The models are expected to approximate real aerodynamic behavior in terms of parasite drag, especially under zero-lift conditions.

TABLE I. MODEL PARAMETERS AND SPECIFICATIONS OF THE SELECTED UAVS

UAVs	Weight (kg)	span (m)	AR	Reference Area (m^2)	Fuselage Length (m)	cruise speed (m/s)	Endurance (h)
1	9	2.9	10.64	0.784	1.9	14	1.5
2	12	3.4	14	0.82	1	17	2
3	7.8	3	17	0.53	0.6	17	1.5
4	6.5	2.2	6	0.8	0.7	20	2
5	7	2.8	10	0.8	1.4	14	2.5
6	4.5	3.2	9.4	1.08	2.15	20	2
7	5	2	8	0.5	1.25	14	1
8	13	3	6	1.4	0.9	20	2
9	9	2.9	11	0.8	1.93	17	1

B. Induced-Drag Elimination via Symmetric Airfoils

The objective of this study is to determine the zero-lift drag coefficient of each UAV configuration. However, CFD simulations directly provide the total drag, which consists of both parasite drag and induced drag. Therefore, a procedure is required to isolate the parasite drag component.

Two main approaches have been reported in the literature. The first approach [12] employs the original cambered airfoils and estimates the parasite drag by subtracting the induced drag from the total drag.

In this method, the total drag is obtained from high-fidelity CFD simulations, while the induced drag is calculated separately using a lower-order aerodynamic tool such as VSPAERO [22]. Although this approach preserves the actual wing geometry, it requires detailed airfoil information for each UAV, which is often unavailable for publicly documented platforms. Furthermore, combining high-fidelity and low-fidelity aerodynamic methods introduces additional uncertainty into the drag decomposition process.

The second approach consists of replacing the original lifting surfaces with symmetric airfoils and imposing a zero angle of attack. Under these conditions, the generated lift is negligible and the induced drag contribution is effectively eliminated, allowing the computed drag to closely represent the parasite drag alone.

Replacing a cambered airfoil with a symmetric one modifies the pressure distribution over the wing and may introduce a small error in the lift-independent drag. Studies have shown that a three-dimensional wing equipped with a cambered airfoil generally exhibits a slightly higher lift-independent drag than an equivalent wing using a symmetric airfoil. Nevertheless, according to Götten [16], the resulting influence on the total drag is generally limited and does not exceed approximately 3%. Given this relatively small error, and considering the lack of reliable airfoil data for several UAVs investigated in this study, the second approach was adopted. Based on the typical thickness of lifting surfaces in mini-UAV configurations, the symmetric NACA 0012 airfoil was assigned to all wing surfaces, while NACA 0009 airfoil was selected for the tail surfaces.

C. Numerical Simulation Methodology

The Computational Fluid Dynamic (CFD) analyses were carried out using ANSYS Fluent, based on the steady Reynolds-Averaged Navier–Stokes (RANS) equations. The k-ω SST turbulence model was employed, as it is widely recommended for low-speed external aerodynamic flows due to its robustness in capturing near-wall effects [23].

The fluid domain was defined as a parallelepiped of size that extended 25 times the maximum body length in flow direction and 15 times perpendicular. The following boundary conditions were applied:

- Velocity inlet corresponding to the UAV cruise speed (see Table I);
- Pressure outlet at atmospheric conditions;
- Symmetry plane along the vertical boundaries;
- No-slip wall condition on all UAV surfaces.

The freestream velocity corresponded to the UAV's cruise speed at zero angle of attack and mean sea level conditions. A turbulence intensity of 1% and a viscosity ratio of 10 were applied at the inlet, representing low-altitude atmospheric conditions. The main numerical simulation parameters are summarized in Table II.

The computational mesh was generated using Fluent Meshing, employing an unstructured poly-hexcore topology, combining polyhedral and hexahedral cells. To accurately resolve wall shear forces, a smooth-transition offset inflation scheme was used with 10 boundary layers and a transition ratio of 0.1. The near-wall spacing was adjusted to maintain a Y+ value around 1, ensuring accurate boundary layer resolution.

The freestream flow was assumed incompressible, consistent with low-speed UAV flight. A coupled solver was used for pressure-velocity coupling. Simulations were initialized using a first-order upwind scheme to ensure stability, and then refined using a second-order upwind scheme for improved accuracy. The drag and lift coefficients were monitored to assess convergence. In cases of delayed convergence, relaxation factors were manually adjusted, or the mesh was locally refined and regenerated.

A mesh-independence study was conducted by progressively increasing the number of cells until the variation in drag coefficient between successive mesh levels was less than 1%. Figs. 2 and 3 illustrate, respectively, the surface mesh and the mesh-convergence curve for UAV 8. Depending on the UAV configuration, the final computational meshes contained between 10 and 20 million cells. The simulation strategy followed the CFD best-practice recommendations reported in Refs [23, 24].

TABLE II. NUMERICAL SIMULATION PARAMETERS

Parameter	Value
Turbulence model	SST *k-ω*
Solver type	Pressure-based
Flow regime	Steady
Pressure-velocity coupling	Coupled
Spatial discretization	Second-order upwind
Turbulence intensity	1%
Viscosity ratio	10
Convergence criterion	residual = 0.001
Target Y+	~1

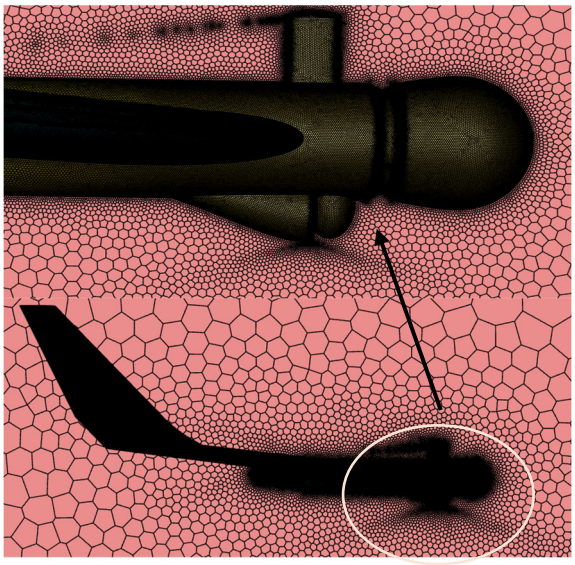

Fig. 2. Mesh discretization and boundary layer for UAV8.

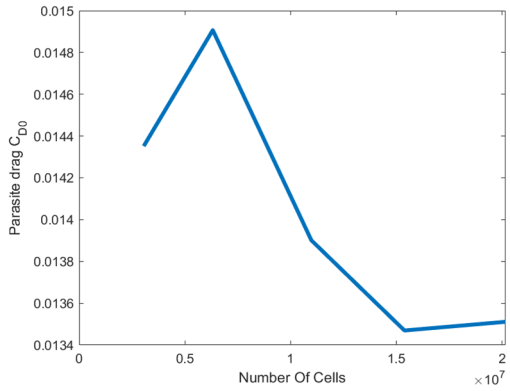

Fig. 3. Mesh convergence study for UAV8.

D. Conceptual Design Framework for Small Electric UAVs

1) Design process

The conceptual design process follows an iterative methodology, as illustrated in Fig. 4. This framework begins with constraint analysis [25, 26], proceeds through initial weight estimation [17], then the required power and wing reference area are derived from the constraint analysis results. Empirical correlations [27] were used to define detailed geometric parameters. Once an initial layout is established, the wetted area is computed and used to estimate parasite drag coefficient via the equivalent skin friction method, The design process then returns to step 1 with the updated drag, iterating until the wetted area converges.

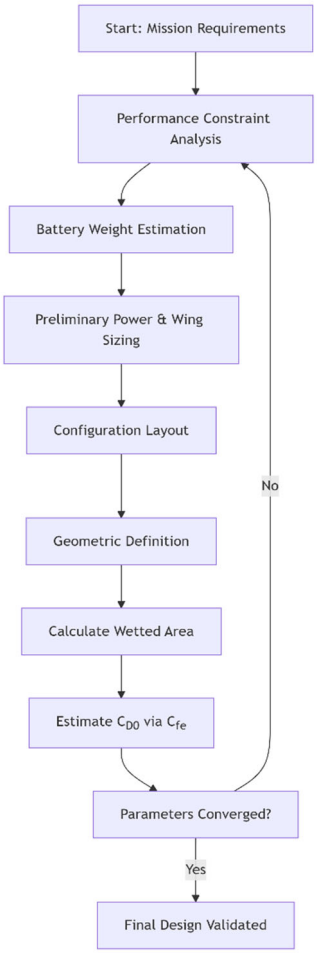

Fig. 4. Diagram process of conceptual design.

2) Battery-powered weight estimation

For electric UAVs, the battery mass fraction is a critical sizing parameter. The methodology of Raymer is adapted here for battery mass estimation across mission segments. For the present study, the climb phase is neglected due to the low service ceiling (≈ 300 m), which results in negligible climb energy relative to cruise and loiter.

The battery mass fractions for loiter and cruise are given by:

$$MFB_{Loiter} = Eg\frac{V_{loiter}}{3.6E_{sb}h_p(\frac{L}{D})} \quad (1)$$

$$MFB_{Cruise} = \frac{Rg}{3.6E_{sb}h_p(\frac{L}{D})} \quad (2)$$

where:
E = endurance (hours);
R = range (km);
g = gravitational acceleration (m/s²);
V_{loiter} = loiter speed (km/h);
$\frac{L}{D}$ = aerodynamic efficiency;
h_p = propeller efficiency;
E_{sb} = battery specific energy (Wh/kg).

In the initial design stage, the aerodynamic efficiency $\frac{L}{D}$ is unknown and is approximated by the maximum lift-to-drag ratio [28]:

$$\left(\frac{L}{D}\right)_{MAX} = \frac{1}{2\sqrt{\left(\frac{C_{D0}}{\pi eAR}\right)}} \quad (3)$$

where C_{D0} is the zero-lift drag coefficient, e is the Oswald efficiency factor, and AR is the wing aspect ratio.

The loiter speed which represent the speed for minimum power is given by the formula [29]:

$$V_{loiter} = 3.6\sqrt{\frac{2}{\rho}\left(\frac{W}{S}\right)\sqrt{(3C_{D0}/(\pi eAR)}} \quad (4)$$

where $\frac{W}{S}$ represent the wing loading and it is determined from constraint analysis following the approach in Ref. [30].

III. Result and Discussion

A. Numerical Simulation Result and Discussion: Surface Pressure Distribution and Drag Coefficient

Figs. 5–7 present the surface pressure distributions of the reconstructed UAVs, grouped according to their cruise speeds (14, 17, and 20 m/s). Within each group, a common pressure legend is adopted to facilitate direct comparison between configurations operating under similar flight conditions. Because the UAVs were simulated at different cruise speeds, the pressure contours are not intended for direct quantitative comparison of absolute pressure magnitudes across different groups. Instead, they provide a qualitative assessment of the flow topology, identify regions of high and low pressure, and highlight the principal aerodynamic features governing parasite drag. For UAV 1, UAV 5, and UAV 7 (Fig. 5), the pressure field exhibits the characteristic stagnation region at the nose, followed by strong suction over the wing surfaces. The most pronounced low-pressure regions are located near the wing–fuselage junction, where the interaction between the lifting surface and the fuselage modifies the local pressure field. These interference effects locally increase the pressure gradients and contribute to the pressure-drag component, although their influence remains limited because they occupy only a small portion of the total wetted area. For UAV 2, UAV 3, and UAV 9 (Fig. 6), the twin-boom configurations (UAV 2 and UAV 3) exhibit additional low-pressure regions at the wing–boom and boom–tail intersections due to the presence of multiple component junctions. These regions indicate increased aerodynamic interference compared with the conventional configurations. In contrast, UAV 9 shows a smaller, weaker high-pressure region at the nose because its nose is narrow and pointed rather than blunt, allowing air to flow around it more smoothly and reducing the size of the high-pressure area. For UAV 4, UAV 6, and UAV 8 (Fig. 7), the tailless flying-wing configuration of UAV 4 exhibits a continuous suction region along the swept leading edge rather than localized suction at discrete component junctions. The absence of a conventional fuselage–tail arrangement minimizes interference effects and contributes to a smoother pressure distribution. Similarly, UAVs 6 and 8 exhibit their primary low-pressure regions above the nose and around the wing root, reflecting the dominant aerodynamic influence of the lifting surfaces over the compact airframe geometry.

Overall, the pressure contours exhibit the characteristic flow pattern of subsonic fixed-wing aircraft, comprising a high-pressure stagnation region near the nose, low-pressure suction regions over the lifting surfaces, and gradual pressure recovery toward the trailing edges.

Fig. 5. Surface pressure contours of UAV 1, UAV 5, and UAV 7 with a common pressure legend (Cruise speed: 14 m/s).

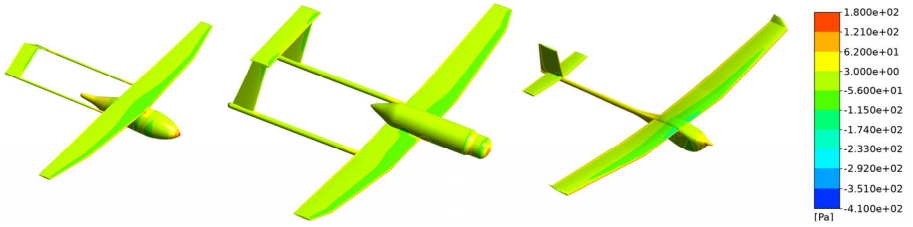

Fig. 6. Surface pressure contours of UAV 2, UAV 3, and UAV 9 with a common pressure legend (Cruise speed: 17 m/s).

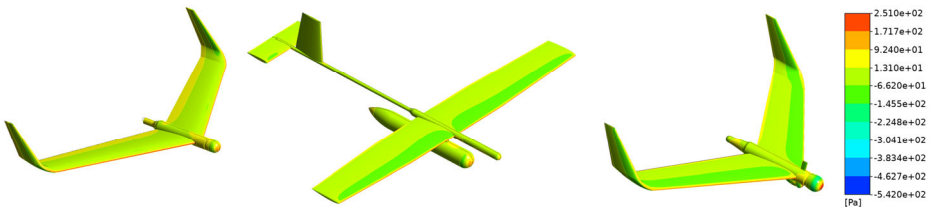

Fig. 7. Surface pressure contours of UAV 4, UAV 6, and UAV 8 with a common pressure legend (Cruise speed: 20 m/s).

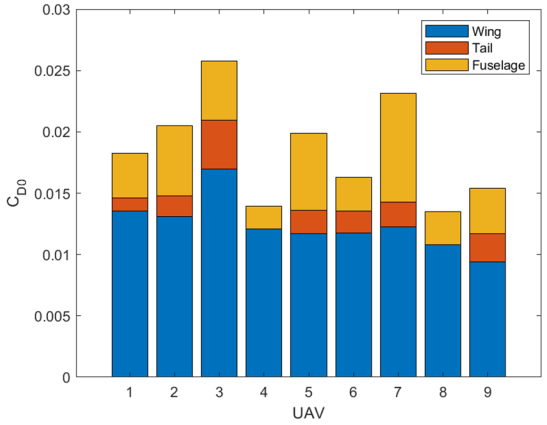

Fig. 8. Drag coefficient for with components distribution different UAVs.

Fig. 8 presents the drag coefficients obtained from the CFD simulations, which range from 0.013 to 0.026. Although the pressure contours shown in Figs. 5–7 provide a qualitative assessment of the aerodynamic flow features, the overall aerodynamic performance of the investigated UAVs is quantitatively evaluated using the drag coefficients presented in Fig. 8. UAV 3 exhibits the highest drag coefficient because its twin-boom configuration introduces multiple wing–boom and boom–tail junctions, increasing aerodynamic interference and the pressure-drag component. In contrast, UAVs 4 and 8, which employ tailless or blended swept-wing configurations, achieve the lowest drag coefficients owing to their smoother geometric transitions and reduced interference effects. Although UAV 8 exhibits a slightly greater fuselage drag contribution than UAV 4 because of the presence of an external antenna and electro-optical turret, both configurations remain aerodynamically more efficient than the conventional layouts.

The relative contributions of the wing, fuselage, and tail to the total minimum drag are presented in Fig. 9. On average, the wing accounts for approximately 61.7% of the total drag, while the fuselage and tail contribute 25.6% and 12.7%, respectively. This distribution differs significantly from that reported by Götten *et al.* [16] for short- to medium-range UAVs, where the wing represents only 27% and the fuselage contribute 17% and the landing gear alone contributed up to 28% of the total drag. In mini UAVs, the absence of landing gear, combined with compact airframe geometries, shifts the dominant source of drag toward the wing.

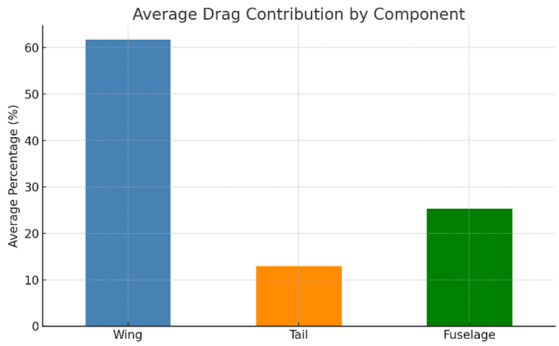

Fig. 9. Component drag distribution.

B. CFD-Derived Equivalent Skin-Friction Coefficient

According to Raymer, the minimum drag can be expressed as the product of the equivalent skin-friction coefficient and the ratio of reference area to wetted area. The equivalent skin-friction coefficient is therefore determined using the following equation:

$$C_{f_e} = C_{D_0} \frac{S_{ref}}{S_{wet}} \tag{5}$$

In this study, the drag coefficients obtained from CFD are considered as minimum (parasite) drag, as the induced drag component has been eliminated following the approach presented in Section II.B.

The equivalent skin friction coefficients C_{f_e} for the nine UAVs are presented in Fig. 10. The values range from 0.0056 to 0.008, with an average of 0.0064. This average is 16%–42% higher than the typical value proposed by Raymer for light general aviation aircraft, respectively single-engine and twin-engine, and 42% lower than the value proposed by Gotten for short- to medium-range UAVs. This indicates that the aerodynamics of mini UAVs is reflecting lower Reynolds numbers, smoother aerodynamic surfaces due to simpler manufacturing, and the absence of drag-intensive components such as landing gear. The results also highlight the inadequacy of applying SMR coefficients to mini (small) UAVs, which can lead to substantial overestimation of parasite drag during conceptual design. The scope of this study is limited to fixed-wing electric mini UAVs intended for close-range missions. Micro UAVs, VTOL configurations, and larger tactical or military UAVs are outside the scope of the present investigation. Consequently, the proposed equivalent skin-friction coefficient should be interpreted as applicable only to this specific class of UAVs.

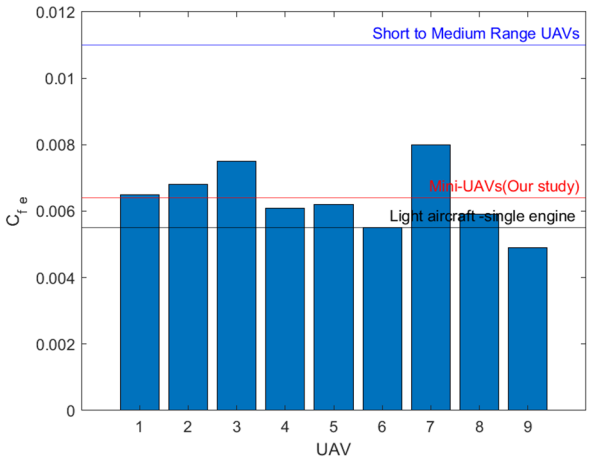

Fig. 10. The equivalent skin friction coefficient for Small/Mini UAVs.

C. Case Study: Impact of Equivalent Skin Friction Coefficient on conceptual Design Outcomes

To quantify the influence of the equivalent skin friction coefficient on UAV conceptual design, a case study was conducted using the requirements summarized in Table III, the mission profile and general configuration are illustrated in Figs. 11 and 12.

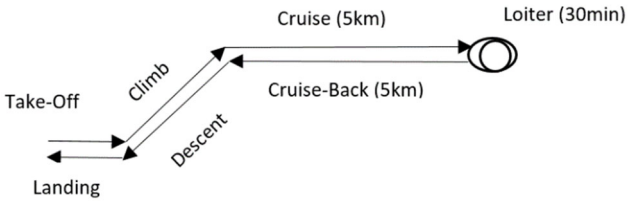

Fig. 11. UAV mission profile.

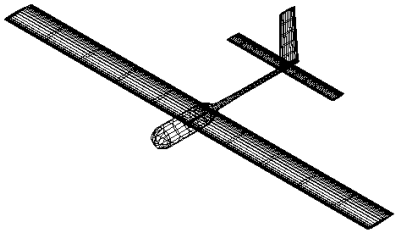

Fig. 12. UAV typical configuration.

TABLE III. DESIGN PARAMETERS AND SPECIFICATIONS OF CASE STUDY

Specification	Value	Unity
Endurance	0.5	Hours
Range	10	km
Maximum speed	36	m/s
Rate of climb	3	m/s
Stall speed	13	m/s
Service ceiling	300	Meters
Maximum takeoff distance	60	m
Payload	1.3	kg

Two sizing cases were analyzed using the same design methodology but different values for the equivalent skin friction coefficient C_{f_e}:

- Case 1 uses the proposed coefficient derived from this study;
- Case 2 uses the Götten coefficient representative of SMR UAVs.

The results are presented in Table IV. Significant differences are observed between the two sizing outcomes. These differences are not negligible. Such variations in key design parameters during the early sizing stage can propagate through the entire development process—affecting structure, propulsion, endurance, and mission feasibility. This underscores the critical importance of using an appropriate C_{f_e} tailored to the specific UAV class.

TABLE IV. PRELIMINARY SIZING COMPARISON FOR CASE 1 AND CASE 2

Case	Power (W)	Surface Area (m²)	MTOW (kg)	C_{f_e}
Case 1	624	0.65	8.67	0.0064
Case 2	904	0.52	9.44	0.011
Error(1/2)	+45%	–20%	+9%	-

IV. CONCLUSIONS

This study derived a dedicated equivalent skin-friction coefficient for small electric fixed-wing UAVs through steady RANS CFD simulations of nine representative configurations. The UAV models were reconstructed from publicly available geometric data and analyzed under zero-lift cruise conditions to isolate the parasite drag component.

The results indicate that the derived equivalent skin-friction coefficient is substantially lower than previously reported values for short- to medium-range UAVs, indicating that the direct application of existing values may not be appropriate for mini electric UAVs. To evaluate the practical implications of the proposed coefficient, a conceptual design case study was performed. The results demonstrated that the use of coefficients developed for larger UAV categories leads to a substantial overestimation of parasite drag, resulting in oversized wing and propulsion system requirements.

The proposed equivalent skin-friction coefficient therefore provides a more representative basis for parasite drag estimation during the conceptual design of small electric UAVs and can improve the accuracy of preliminary sizing methodologies. Future work should focus on experimental validation of the CFD results through wind-tunnel testing of representative UAV configurations and on extending the database to include a broader range of mini UAV geometries.

CONFLICT OF INTEREST

The authors declare no conflict of interest.

AUTHOR CONTRIBUTIONS

S.M.S.M: Conceptualization, methodology, software, investigation, formal analysis, data curation, visualization, writing—original draft, and writing—review and editing. M.E.A.A: Supervision, methodology, validation, and writing—review and editing. All authors had approved the final version.

REFERENCES

[1] S. Overall. (May 2025). Electric Unmanned Aerial Vehicle (E-UAV) Market Analysis. *Technavio*. [Online]. Available: https://newsroom.technavio.org/electric-unmanned-aerial-vehicle-e-uav-market

[2] M. J. Logan, J. Chu, M. A. Motter, D. L. Carter, M. Ol, and C. Zeune. (May 2007). Small UAV Research and Evolution in Long Endurance Electric Powered Vehicles. *NASA Technical Reports Server (NTRS)*. [Online]. Available: https://ntrs.nasa.gov/citations/20070021697

[3] J.-H. An, D.-Y. Kwon, K.-S. Jeon, M. Tyan, and J.-W. Lee, "Advanced Sizing Methodology for a Multi-Mode eVTOL UAV Powered by a Hydrogen Fuel Cell and Battery," *Aerospace*, vol. 9, no. 2, 71, 2022. doi: 10.3390/aerospace9020071

[4] K. Cong, D. Ma, X. Xia, Y. Cheng, H. Guan, and B. Zhao, "A novel sizing methodology for fixed-wing VTOL UAVs considering constraint on minimum transition time," *Aerospace Science and Technology*, vol. 157, 109838, 2025. doi: 10.1016/j.ast.2024.109838

[5] M. Tyan, N. V. Nguyen, S. Kim, and J.-W. Lee, "Comprehensive preliminary sizing/resizing method for a fixed wing—VTOL electric UAV," *Aerospace Science and Technology*, vol. 71, pp. 30–41, 2017. doi: 10.1016/j.ast.2017.09.008

[6] D. F. Finger, "Comparative performance and benefit assessment of VTOL and CTOL UAVs," in *Deutscher Luft-und Raumfahrtkongress*, 2016, 3.

[7] D. Raymer, *Aircraft Design: A Conceptual Approach*, 5th ed. Washington, DC: American Institute of Aeronautics and Astronautics, Inc., 2012.
[8] J. Roskam, *Airplane Design: Preliminary Sizing of Airplanes*, DARcorporation, 1997.
[9] E. Torenbeek, *Synthesis of Subsonic Airplane Design*, Dordrecht: Springer Netherlands, 1982.
[10] A. Boutemedjet, M. Samardžić, L. Rebhi, Z. Rajić, and T. Mouada, "UAV aerodynamic design involving genetic algorithm and artificial neural network for wing preliminary computation," *Aerospace Science and Technology*, vol. 84, pp. 464–483, 2019. doi: 10.1016/j.ast.2018.09.043
[11] P. Panagiotou and K. Yakinthos, "Aerodynamic efficiency and performance enhancement of fixed-wing UAVs," *Aerospace Science and Technology*, vol. 99, 105575, 2020. doi: 10.1016/j.ast.2019.105575
[12] F. Goetten, M. Havermann, C. Braun, F. Gómez, and C. Bil, "On the Applicability of Empirical Drag Estimation Methods for Unmanned Air Vehicle Design," in *Proc. 2018 Aviation Technology, Integration, and Operations Conf.*, Atlanta, 2018, 3192. doi: 10.2514/6.2018-3192
[13] M. Sahraoui, A. Boutemedjet, M. Mekadem, and D. Scholz, "Automated Design Process of a Fixed Wing UAV Maximizing Endurance," *Journal of Applied Fluid Mechanics*, vol. 17, no. 11, pp. 2299–2312, 2024. doi: 10.47176/jafm.17.11.2647
[14] S. Gudmundsson, *General Aviation Aircraft Design: Applied Methods and Procedures*. Butterworth-Heinemann, 2022.
[15] G. W. H. V. Es, "Rapid Estimation of the Zero-Lift Drag Coefficient of Transport Aircraft," *Journal of Aircraft*, vol. 39, no. 4, pp. 597–599, 2002. doi: 10.2514/2.2997
[16] F. Götten, D. F. Finger, M. Havermann, C. Braun, M. Marino, and C. Bil, "Full configuration drag estimation of short-to-medium range fixed-wing UAVs and its impact on initial sizing optimization," *CEAS Aeronaut J*, vol. 12, no. 3, pp. 589–603, 2021. doi: 10.1007/s13272-021-00522-w
[17] K. P. Valavanis and G. J. Vachtsevanos, *Handbook of Unmanned Aerial Vehicles*, Springer Publishing Company, Incorporated, 2014.
[18] Alcore Technologies. (2026). Biodrone. [Online]. Available: https://www.alcoretech.com/produit/biodrone/
[19] I. Kemp and D. Lake. (2008). Unmanned Vehicles Handbook 2008. [Online]. Available: https://vdoc.pub/documents/unmanned-vehicles-handbook-2008-4ce6abdg74b0
[20] BAYKAR Technology. (2026). Turkey's first tech company to develop indigenous UAVs. [Online]. Available: https://baykartech.com/en/
[21] R. Austin, *Unmanned Aircraft Systems: UAVS Design, Development and Deployment*. John Wiley & Sons, 2011.
[22] OpenVSP. [Online]. Available: https://openvsp.org/
[23] A. J. Keane, A. Sóbester, and J. P. Scanlan, *Small Unmanned Fixed-wing Aircraft Design: A Practical Approach*, John Wiley & Sons, 2017.
[24] F. Götten, D. Finger, M. Marino, C. Bil, M. Havermann, and C. Braun, "A review of guidelines and best practices for subsonic aerodynamic simulations using RANS CFD," in *Proc. APISAT 2019 Asia Pacific International Symposium on Aerospace Technology*, 2019, pp. 227–245.
[25] M. H. Sadraey, *Design of Unmanned Aerial Systems*. John Wiley & Sons, 2020.
[26] P. L. Bishay *et al.*, "Design and Analysis of MataMorph-3: A Fully Morphing UAV with Camber-Morphing Wings and Tail Stabilizers," *Aerospace*, vol. 9, no. 7, 382, 2022. doi: 10.3390/aerospace9070382
[27] F. Götten, D. F. Finger, C. Braun, M. Havermann, C. Bil, and F. Gómez, "Empirical Correlations for Geometry Build-Up of Fixed Wing Unmanned Air Vehicles," in *Proc. the 2018 Asia-Pacific International Symposium on Aerospace Technology (APISAT 2018)*, 2019, pp. 1365–1381. doi: 10.1007/978-981-13-3305-7_109
[28] J. Gundlach, *Designing Unmanned Aircraft Systems*, American Institute of Aeronautics & Astronautics Reston, VA, 2014.
[29] J. D. Anderson, *Aircraft Performance and Design*, vol. 1. WCB/McGraw-Hill Boston, MA, 1999.
[30] M. H. Sadraey, *Aircraft Design: A Systems Engineering Approach*, John Wiley & Sons, 2024.

Copyright © 2026 by the authors. This is an open access article distributed under the Creative Commons Attribution License which permits unrestricted use, distribution, and reproduction in any medium, provided the original work is properly cited (CC BY 4.0).